



Physical properties and structure of mechanically activated solid solution $\text{Pb}(\text{Zr}_{0.7}\text{Ti}_{0.3})\text{O}_3$

Kamaludin Abdulvakhidov¹ · Ivan Dmitrenko¹ · Alexander Soldatov¹ · Zhengyou Li¹ · Marina Sirota¹

Received: 28 October 2021 / Accepted: 21 December 2021 / Published online: 5 January 2022
© The Author(s), under exclusive licence to Springer-Verlag GmbH, DE part of Springer Nature 2022

Abstract

The ability to control the target physical properties of functional materials without changing stoichiometry and doping is one of the tasks of physical materials science. This work is the first to study the influence of structural defects generated under a force action combined with shear deformation (mechanical activation) on the crystal structure and physical properties of $\text{PbZr}_{0.7}\text{Ti}_{0.3}\text{O}_3$ solid solution. Bridgman's anvils were used to generate structural defects. The symmetry of $\text{PbZr}_{0.7}\text{Ti}_{0.3}\text{O}_3$ was best described by the space group $R3m$. It was found that $\text{PbZr}_{0.7}\text{Ti}_{0.3}\text{O}_3$ is characterized by a non-monotonic change in the unit cell parameters (a and α) of the dislocation density (ρ_D) with an increase in the mechanical activation pressure. By measuring the sizes of coherent scattering regions (D) and microstrains ($\Delta d/d$), it was found that at a mechanical activation pressure of 120 MPa, a recrystallization process develops in mechanically activated powders, leading to the “healing” of the crystal structure. It is shown that by choosing the mechanical activation pressure, one can control the temperature T_m of the maximum of the dielectric permittivity ϵ_m within $\Delta T_m = 11$ °C, the Weiss constant C_W , and the degree of change in the first-order phase transition. The microstructure of the compositions was studied using SEM, the dynamics of the crystal lattice were studied by X-ray diffraction analysis, optical absorption and FTIR-spectroscopy, where the controlled parameters were the root-mean-square static displacements $\sqrt{U_s^2}$, the bandgap E_g and the force constants k . It was found that with a change in the pressure of mechanical activation, E_g changes nonmonotonically within the range of 3.21–3.37 eV.

Keywords PZT · Mechanical activation · Defects · Dielectric permittivity · Bandgap

1 Introduction

Recently, researchers have increased their interest in studying the physicochemical properties of functional materials after various impacts on them. Among these impacts, the mechanical force action combined with shear deformation (mechanical activation) occupies a special place. Mechanical activation on a solid is accompanied by changes in various structural and physical properties, depending on the applied pressure and shear deformation values. What is the activator of such changes? Regardless of the mechanical activation methods, there are several relaxation channels supplied the mechanical energy to the material. Among them, the main ones are heating of the activated body, accumulation

of structural defects (dislocations, point defects), dispersion of the activated body to the nanometer scale, dynamic recrystallization, formation of high-pressure phases, etc. Among the mechanical activation methods, the most accessible is the mechanical activation using Bridgman anvils. It is a “clean” method compared to activation methods using planetary ball mills, vibrating mills and other dispersants, in which material wear of grinding balls and jars takes place. It is also an alternative method for alloying metals such as Fe and Cu, etc., which cannot be done with the conventional alloying methods. We also note the significant advantage of this method is that the stoichiometry of the compositions does not change during mechanical activation.

Among the solids, the class of crystalline bodies with Ferro-piezoelectric properties is the most susceptible to mechanical force action. It was shown in [1–4] that mechanical activation could purposefully change the physical properties of relaxor ferroelectrics, such as $\text{PbIn}_{0.5}\text{Nb}_{0.5}\text{O}_3$, $\text{PbSc}_{0.5}\text{Ta}_{0.5}\text{O}_3$ and $\text{PbFe}_{0.5}\text{Nb}_{0.5}\text{O}_3$. Mechanical activation can lead to a change in the crystallite size [5], formation of

✉ Kamaludin Abdulvakhidov
kgabdulvahidov@sfnedu.ru

¹ Smart Materials Research Institute, Southern Federal University, Sladkova Str. 174/28, Rostov-on-Don, Russia

lattice defects [6, 7], amorphization of crystalline phases [8, 9], and phase transformations [10, 11].

Among Ferro-piezoelectrics, the solid solution system of piezoelectric lead zirconate titanate—[Pb(Zr,Ti)O₃, PZT], stands out because of its wide range of practical applications as infrared and ultrasonic sensors, microdrives and actuators [12–16], due to the possibility of obtaining it by various methods [17–23] and sensitivity to both dopants—compounds and the concentration of the substituted cations in oxygen octahedra [24]. Compositions within a concentration range called the morphotropic region, or compositions adjacent to the boundaries of this region are particularly sensitive to external influences [25–28]. Earlier in [26, 29], experimental results were published with a detailed analysis of the influence of mechanical activation on PZT with the concentration $x=0.42$ and 0.44 . In this work, we chose the composition PbZr_{0.7}Ti_{0.3}O₃. The interest in this composition is because this composition takes us away from the morphotropic region, where two phases coexist but are still far from the orthorhombic phase of PbZrO₃, which is antiferroelectric [30]. Therefore, it is of interest to study the influence of mechanical activation on this composition's structure and physical properties.

2 Experimental details

To obtain the composition of PbZr_{0.7}Ti_{0.3}O₃, oxides of PbO, TiO₂ and ZrO₂ (PbO ≥ 99.0%, TiO₂ ≥ 99.9%, ZrO₂ ≥ 99.9%, Sigma-Aldrich) were taken in stoichiometric proportions. The synthesis was carried out by the “columbite” method, which was divided into 2 stages. At the first stage, ZrO₂ and TiO₂ were mixed and ground in an agate mortar in the presence of ethanol for 2 h, and then sintered in a thermostated muffle furnace at 1150 °C for 2 h. At the second stage, the sintered product was mixed with PbO and ground in an agate mortar for 2 h in the presence of ethanol. The resulting powder was then pressed into a cylinder, placed in a platinum crucible and sintered at 1250 °C for 2 h. To compensate for the partial sublimation of PbO during sintering, PbZrO₃ powder was used as the atmosphere-forming composition. Then, the furnace was turned off and cooled by inertia to room temperature. After cooling the furnace, the composition was ground in an agate mortar for 0.5 h in the presence of ethanol. It was the starting (reference) powder for mechanical activation.

Equal weight portions of this reference powder were placed between the Bridgman's anvils for mechanical activation. The lower anvil rotated at a fixed pressure with an angular velocity of 0.3 rad/min. The range of applied pressures in this work was 80–320 MPa. Within this pressure range, a sufficiently high degree of crystallinity of the activated powder is still preserved, but structural defects are

generated and their type and concentration can be varied. In all these experiments, the parameter ζ , characterizing the shear deformation was about 12. As in [31], its value was determined by the formula:

$$\zeta = \ln\left(\frac{\nu r}{d}\right) \quad (1)$$

where ν is the angle of rotation in radians (in this work $\nu = 12$ rad), r is the radius of the anvil, and d is the thickness of the sample. Then, the mechanically activated samples (which could be in various metastable states) were studied by various methods described below. To study the electrophysical and optical properties, disks with 10 mm in diameter and 1 mm thick were sintered from the powders. Each ceramic sample was sintered from seven portions of mechanically activated powder at 1150 °C for 2 h. The average density of these ceramic samples varied depending on the mechanical activation pressures in the range 7.76–7.82 g/cm³. After each synthesis and sintering process, a D2 PHASER X-ray diffractometer (Bruker) was used to determine the phase composition and structural parameters of each sample, which uses Cu K_{α} radiation ($K_{\alpha 1} = 1.54060$ Å and $K_{\alpha 2} = 1.54443$ Å), with a 2θ step of 0.01° and acquisition time 0.1 s per point. For dielectric measurements, a colloidal silver paste was applied to both sides of the ceramic samples and annealed at $T = 750$ °C for 10 min. The dielectric properties of the samples were analyzed by E7-20 automatic immittance meter (MNIPI, Belarus). Optical absorption spectra were studied on a Shimadzu UV-2600 double-beam spectrophotometer at room temperature. Fourier-transform infrared spectra (FTIR) were recorded on an FSM-1202 Fourier spectrometer (Infraspec, Russia) with a resolution of 2 cm⁻¹. The morphology and microstructure of mechanically activated powders were studied using a scanning electron microscope (Carl Zeiss EVO 40, Germany).

3 Results and discussion

3.1 Structural characterization

Figure 1 shows as an example photomicrographs of the reference and mechanically activated at a pressure of 240 MPa.

Figure 1b shows that larger particles are covered with a loose layer of the smallest particles after mechanical activation. This is due to the electrification of particles by charges accumulated on the surfaces of crystallites (direct piezoelectric effect) during mechanical activation. Almost all mechanically activated samples are a collection of particles ranging in size from tens of nanometers to micrometers. The diffraction patterns of the reference and mechanically activated compositions (see Fig. 2a) were processed by the full-profile Rietveld analysis using the FullProf software

package. It was found that the reference and mechanically activated powders at room temperature are best fitted by the space symmetry group $R3m$.

As shown in Fig. 2b, the mechanical activation leads to a broadening and leftward shift in the diffraction angle 2θ of the Bragg peaks.

Figure 3a shows the dependencies of the unit cell parameters, and Fig. 3b shows the sizes of the coherent scattering regions (D) and the microstrains ($\Delta d/d$) of powder on the applied pressure during mechanical activation. As shown in Fig. 3, a sharp increase in the parameter a and microstrains at a pressure of 80 MPa is due to dislocations and point

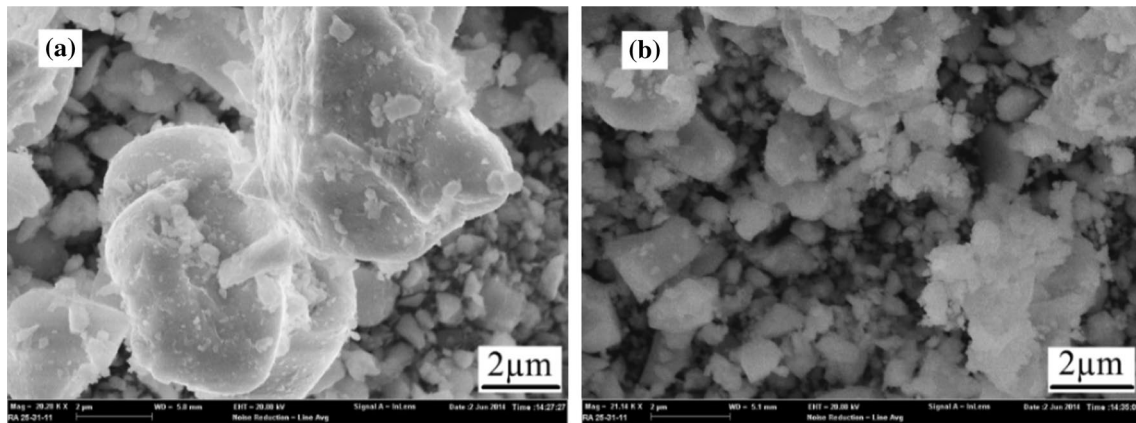


Fig. 1 Scanning electron microscopy images of reference—(a), and mechanically activated $\text{Pb}(\text{Zr}_{0.7}\text{Ti}_{0.3})\text{O}_3$ under a pressure of 240 MPa—(b)

Fig. 2 a Diffraction patterns of the reference and mechanically activated powder samples of $\text{Pb}(\text{Zr}_{0.7}\text{Ti}_{0.3})\text{O}_3$, b the selected angular interval

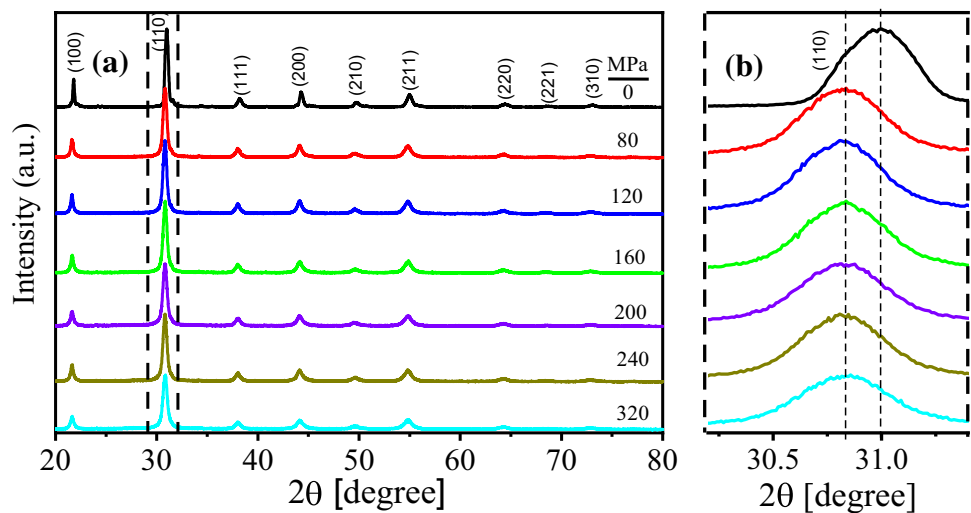
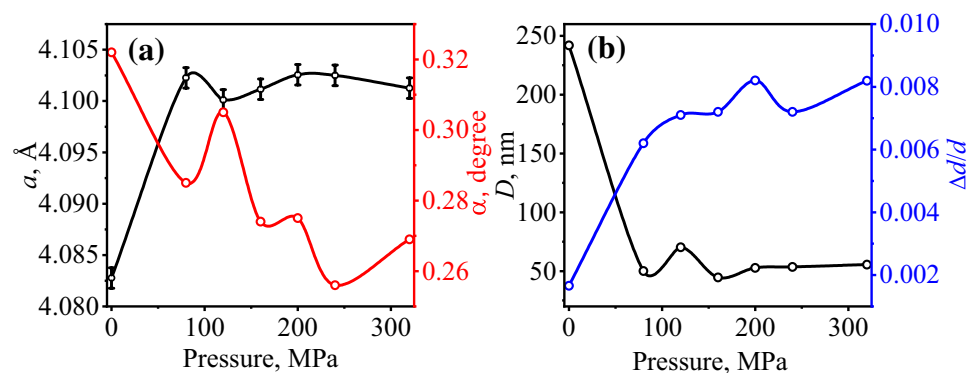


Fig. 3 Dependencies of the linear a and angular α parameters of the unit cell—(a); the size of the coherent scattering region D and microstrains $\Delta d/d$ —(b) of the reference and mechanical activated $\text{PbZr}_{0.7}\text{Ti}_{0.3}\text{O}_3$ powder samples on the mechanical activation pressure



defects accumulated in the crystal lattice during mechanical activation.

As expected, D and the rhombohedral angle α also decrease sharply at this pressure. However, a further increase in the applied pressures is accompanied by a non-monotonic behavior of these parameters. A small jump in D and α , as well as a decrease in a at a processing pressure $P = 120$ MPa, is due to the “healing” of the crystal lattice. Ballistic diffusion processes that develop in mechanically activated compositions at a specific mechanical activation pressure can lead to recrystallization processes, accompanied by the absorption of “weak” defective grains by “healthier” grains [30, 32]. This process develops at a pressure of 120 MPa. Note that these pressures differ for different compositions.

A further increase in mechanical activation pressure leads to an insignificant increase in microstrains. The sizes D also stabilize at about 50 nm, which, in our view, is the marginal size for this mechanoactivation pressure range for $\text{PbZr}_{0.7}\text{Ti}_{0.3}\text{O}_3$. Such processing of the synthesized powders at different pressures indicates their various metastable states. Consequently, ceramics sintered under the same environment have different starting conditions. Quantitative control of point defects in powder samples is practically impossible, but they can be qualitatively estimated from diffractometric data. Therefore, in this work, we calculated only the dislocation densities ρ_D , which are given in Table 1. The calculation of ρ_D was carried out using the following formula:

$$\rho_D = 3nD^{-2} \quad (2)$$

For $n = 1$, under the assumption that the network of dislocations coincides with the grain boundaries, and large distances imply an almost complete absence of interaction between these dislocations [33].

As shown in Table 1, an increase in the mechanical activation pressure to 120 MPa leads, after a sharp increase at 80 MPa, to a twofold decrease in the dislocation density.

The maximum dislocation density is observed at 160 MPa, but subsequently, we observe a monotonic decrease in ρ_D . A pressure of 160 MPa is a threshold pressure, after which point defects play a predominant role in the generated structural defects.

3.2 Lattice dynamics

3.2.1 Root-mean-square static displacements

As mentioned above, the dissipation of the external mechanical energy supplied to the sample during its deformation is carried out through various channels. A significant part of this energy is spent on generating static distortion. Static distortions caused by the displacement of atoms from their normal positions should have the same effect as the displacement of atoms during thermal vibrations. They, like dynamic displacements, lead to a decrease in the integrated intensities of the diffractograms, which is caused by an increase in the number of ions located in the “dislocated” regions of the crystal lattice [34]. Static distortion cannot exist apart from dynamic distortion. Consequently, both factors influence the intensity of the X-ray diffraction profiles. Earlier in [35], we studied the influence of mechanical activation on the RMS displacement \bar{U}^2 and the Debye temperature of the $\text{PbZr}_{0.56}\text{Ti}_{0.44}\text{O}_3$ solid solution from the morphotropic region. It was found that these parameters can be significantly varied by changing the concentration of structural defects.

To calculate the RMS static displacements \bar{U}_s^2 , we use the formula:

$$\bar{U}_s^2 = \frac{3a^2}{4\pi^2[h^2 + k^2 + l^2]} \ln \left[\frac{I_{\text{ref}}}{I_{\text{act}}} \right] \quad (3)$$

where a —the cell parameter, I_{ref} and I_{act} —the integrated intensities corresponding to the reflecting planes with Miller indices (220) of the reference and mechanically activated samples. The above formula is valid for the cubic system when measured with a sensitive detector and stable X-ray radiation. Therefore, the integrated intensities of the selected Bragg reflections were measured at 400 °C to exclude the anisotropy of thermal vibrations of the crystal lattice. The scanning time of each peak from “baseline to baseline” at this temperature was 120 s, which practically did not affect the diffusion processes in the powders. Figure 4 shows the graphs of the dependency of $\sqrt{\bar{U}_s^2}$ on the mechanical activation pressure.

As shown in Fig. 4, $\sqrt{\bar{U}_s^2}$ of mechanically activated samples grow with increasing pressure of mechanoactivation. The growth of $\sqrt{\bar{U}_s^2}$ should lead to an increase in the linear parameter a of the unit cell. With an increase in pressure to 200 MPa, we observe a change in a and D correlated with $\sqrt{\bar{U}_s^2}$. However, after 240 MPa, we have maximum and stable values of

Table 1 The dislocation densities of $\text{PbZr}_{0.7}\text{Ti}_{0.3}\text{O}_3$

P , MPa	0	80	120	160	200	240	320
ρ_D , 10^9 cm^{-2}	5.13	119.5	60.7	150.1	108.0	104.8	97.4

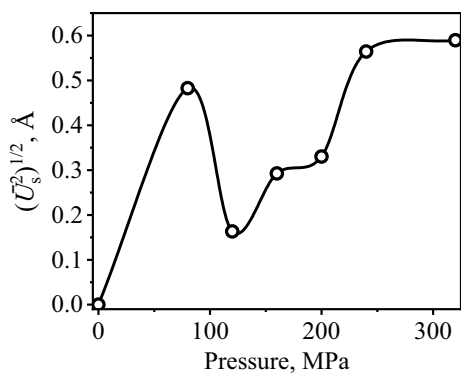


Fig. 4 Dependencies of the RMS static displacements $(\overline{U_s^2})^{1/2}$ on the mechanical activation pressures

both $\sqrt{\overline{U_s^2}}$ and a and D , indicating that structural defects have reached their saturation.

3.2.2 Optical spectra

The bandgap (E_g) is a parameter that depends on many factors, including the structural perfection of the crystalline body. Since ceramic samples of $\text{PbZr}_{0.7}\text{Ti}_{0.3}\text{O}_3$ constitute a structure obtained from the powders in metastable states, it is of interest to study the influence of mechanical activation on E_g . For this purpose, the intrinsic optical absorption of reference and mechanically activated samples were studied. To estimate the bandgap, we used the methods described in [36–38] and calculated the Kubelka–Munk function $F(R)$. Then, using the Kubelka–Munk function $(h\nu \cdot F(R_\infty))^2$, the $(E \cdot F(R_\infty))^2$ dependencies are plotted as a function of $h\nu$. The corresponding plots for these two samples are shown

in Fig. 5, and the absorption characteristics of the reference (Fig. 5a) and mechanically activated samples at 240 MPa (Fig. 5b) are different.

The calculated bandgaps E_g of the reference and mechanically activated $\text{Pb}(\text{Zr}_{0.7}\text{Ti}_{0.3})\text{O}_3$ ceramic samples at room temperature are shown in Table 2. As shown in Fig. 5 and Table 2, mechanical activation leads to a non-monotonic change in the ceramic samples' bandgaps.

3.2.3 FTIR-spectroscopy

Fourier-transform infrared spectroscopy (FTIR) has been used for decades to study ferroelectric phase transitions in perovskites [39]. This vibrational method was used to reveal the influence of mechanical activation on the physical properties of the $\text{PbZr}_{0.7}\text{Ti}_{0.3}\text{O}_3$ ceramics. Figure 6 shows the normalized FTIR spectra of the reference and mechanically activated samples in the spectral range of 400–750 cm^{-1} . The selected interval is sufficient to describe the vibrational profile of the perovskite unit cell. In the range of 400–750 cm^{-1} , an absorption band of a complex shape is observed, consisting of valence modes of the Ti–O and Zr–O bonds in the BO_6 octahedra. The complex and asymmetric strip profiles in Fig. 6 indicate a certain composition of the two isolated spectra of PbZrO_3 and PbTiO_3 , PbZrO_3 gives a pair of bands with maxima at 738 and 554 cm^{-1} , and PbTiO_3 gives a pair of bands with maxima at 700 and 562 cm^{-1} [40]. It is known that the TiO_6 octahedron has four different vibration modes: ν_1 —stretching at higher frequencies, and ν_2 —torsion, ν_3 —bending and ν_4 —cationic (TiO_3) vibration at lower frequencies [41]. The experimental profiles were fitted according to the least-square method using three Gaussian curves to identify the vibrational components. The fitting results are shown in Fig. 6; the maxima of the components are 632, 559,

Fig. 5 Kubelka–Munk transformed reflectance spectra of the reference (a) and mechanically activated (b) $\text{PbZr}_{0.7}\text{Ti}_{0.3}\text{O}_3$ ceramics at 240 MPa

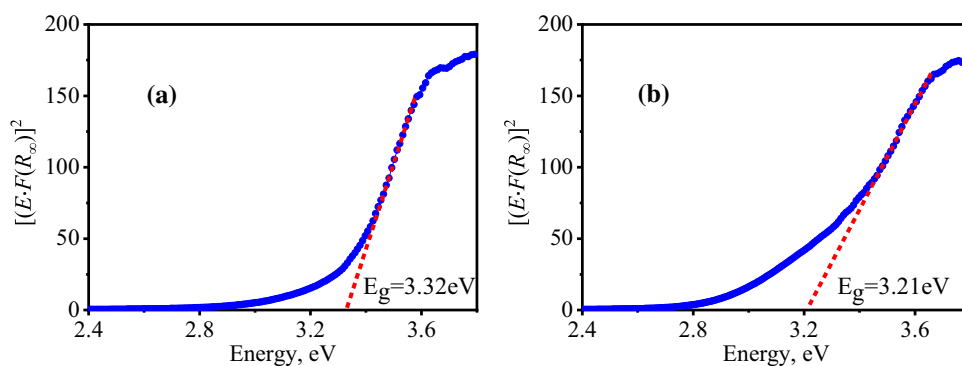
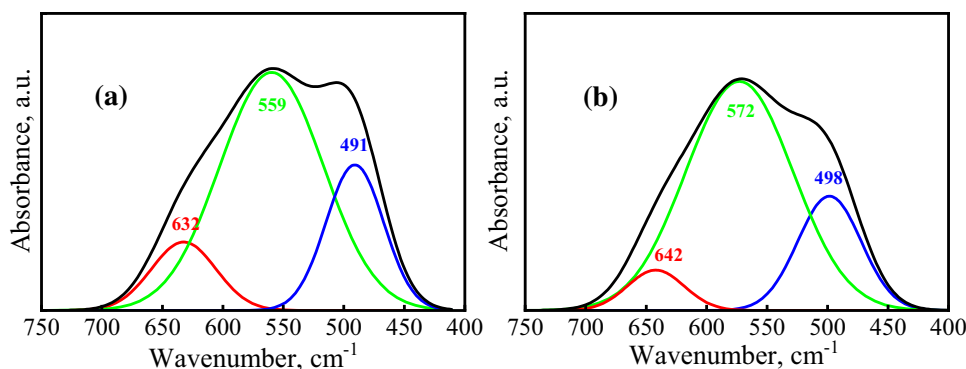


Table 2 The dependencies of the bandgaps of $\text{Pb}(\text{Zr}_{0.7}\text{Ti}_{0.3})\text{O}_3$ on the mechanical activation pressures

P , MPa	0	80	120	160	200	240	320
E_g , eV	3.32	3.37	3.32	3.24	3.33	3.21	3.36

Fig. 6 FTIR spectra of the reference (a) and mechanically activated (b) samples ($\text{PbZr}_{0.7}\text{Ti}_{0.3}\text{O}_3$) at 240 MPa



491 cm^{-1} for the reference sample, and $642, 572, 498\text{ cm}^{-1}$ for the mechanically activated samples. It shows that all three components for the mechanically activated samples are shifted by 10, 13, and 7 cm^{-1} to higher frequencies (blue shift). Since $\nu_2, \nu_3,$ and ν_4 are below 400 cm^{-1} [42], the observed vibrational components can be attributed to the ν_1 -stretching modes of Ti–O and Zr–O bonds in the BO_6 octahedron of the ABO_3 structure [43].

Next, we studied the dependencies of the force constants of the Ti–O and Zr–O bonds on the mechanical activation pressures using the formula:

$$\tilde{\nu} = (1/2\pi c)\sqrt{k/\mu} \quad (4)$$

where $\tilde{\nu}$ —the wavenumber, c —the speed of light, k —the average force constant, μ —the reduced mass. The calculation results are shown in Table 3.

Table 3 shows that the changes of $\tilde{\nu}$ and k are non-monotonic; however, these values for the mechanically activated samples are higher than those of the reference sample.

3.3 Dielectric properties

The dielectric properties of perovskite structure oxides depend on the presence of various types of defects and external factors. Therefore, the dielectric properties can be attributed to structure-sensitive properties. Let us consider the

role of structural defects in forming the dielectric properties of $\text{Pb}(\text{Zr}_{0.7}\text{Ti}_{0.3})\text{O}_3$, for which, as an example, we present a composition obtained from a powder mechanically activated at a pressure of 240 MPa. However, there is no fundamental difference between it and other samples obtained at other pressures.

Figure 7a, a' show the temperature dependencies of the real part of the dielectric permittivity $\epsilon'(T)$ of the reference and mechanically activated $\text{Pb}(\text{Zr}_{0.7}\text{Ti}_{0.3})\text{O}_3$ samples at 240 MPa, and in Fig. 7b, b' the corresponding Cole–Cole diagrams of complex quantities of electrical modulus. After mechanical activation, the temperature of the maximum dielectric permittivity at a frequency of 1 kHz increases from $T_m = 384\text{ }^\circ\text{C}$ to $T_m = 389\text{ }^\circ\text{C}$, and the phase transition is blurred.

The combination of these effects can be explained using the mechanism of depleted Schottky layers, which are the characteristic both for the metal-dielectric boundaries and crystallite boundaries with their bulk in polycrystals [44, 45]. The depleted layers formed in polycrystals obtained from mechanically activated powders lead to a significant difference in dielectric spectra from Debye's ones. Their main characteristics are similar to the spectra of static mixtures [46].

Figure 7b, b' show the Cole–Cole diagrams—the dependencies of the imaginary part of the electrical modulus $M''(\omega)$ on the real part of the electrical modulus $M'(\omega)$ of the same

Table 3 Dependencies of the average force constants of the Ti–O and Zr–O bonds of the $\text{PbZr}_{0.7}\text{Ti}_{0.3}\text{O}_3$ ceramics

Pressure (MPa)	Ti–O stretching-1 (cm^{-1})	Force Constant (N/m)	Ti–O stretching-2 (cm^{-1})	Force Constant (N/m)	Zr–O stretching (cm^{-1})	Force Constant (N/m)
0	632	312.9	560	245.7	491	188.9
80	639	319.9	568	252.7	496	192.7
120	639	319.9	570	254.5	497	193.5
160	637	317.9	569	253.6	498	194.3
200	640	320.9	571	255.4	497	193.5
240	637	317.9	568	252.7	496	192.7
320	642	322.9	573	257.2	498	194.3

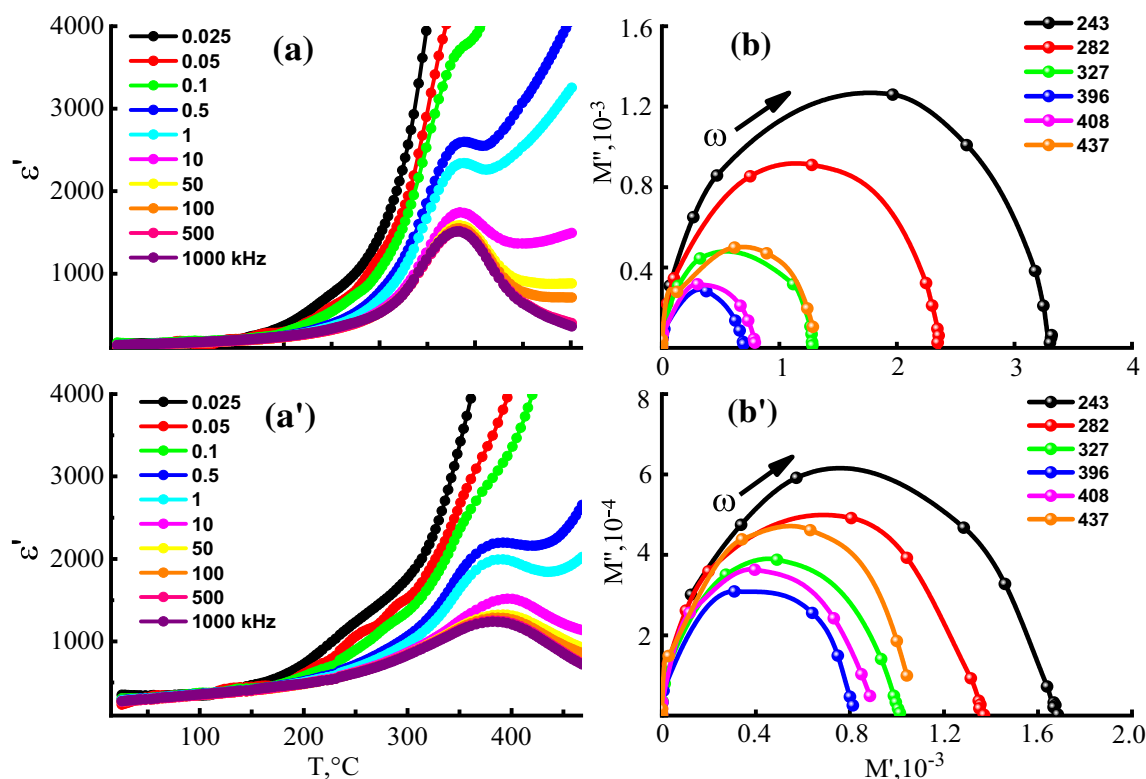


Fig. 7 The temperature dependencies of ϵ and Cole–Cole plots of the electric modulus $M^*(\omega)$ of the reference (a), (b) and mechanically activated (a'), (b') $\text{PbZr}_{0.7}\text{Ti}_{0.3}\text{O}_3$ ceramics at 240 MPa

samples at different temperatures. The appearance of an arc in the spectrum at a certain temperature confirms the single-phase nature of the materials. The large value of ϵ_s is due to charge accumulation on the crystallite–depleted Schottky layers of ceramic. The thickness of the weakly conductive layers between the more conductive ceramic crystallites should be significantly smaller than the sizes of the crystallites. Single semicircular arcs in Fig. 7b, b' show a predominant contribution of grain volume. As seen from Fig. 7b', mechanical activation leads to some decrease in the contribution of grain volume.

The frequency–temperature dependencies of the electrical modulus $M'(\omega)$ and $M''(\omega)$ of the reference and mechanically activated $\text{PbZr}_{0.7}\text{Ti}_{0.3}\text{O}_3$ samples are shown in Fig. 8a, b and Fig. 8a', b'. As shown in Fig. 8a, b, the value of $M'(\omega)$ increases with increasing frequency but decreases with increasing applied pressure. Fig. 8a', b' show that the imaginary part of the modulus $M''(\omega)$ of $\text{PbZr}_{0.7}\text{Ti}_{0.3}\text{O}_3$, regardless of temperature, has a single relaxation time determined by the formula:

$$\tau = \frac{1}{2\pi f_m} \quad (5)$$

where f_m —the frequency of the maximum of $M''(\omega)$.

The frequency range to the left of maximum $M''(\omega)$ determines the range in which charge carriers are mobile at large distances; to the right of maximum $M''(\omega)$, the movement of carriers is limited by a potential well, and they are mobile at shorter distances [47]. Noted that the observed peak of $M''(\omega)$ is not symmetric. This indicates a non-Debye type of relaxation in the samples. Moreover, increasing temperature leads to a shift of the peaks to higher frequencies. Therefore, the relaxation is temperature dependent [48]. Moreover, as shown in Fig. 8b', mechanical activation leads to a decrease in the $M''(\omega)$ values and a shift of the peaks toward lower frequencies.

Since dielectric permittivity relaxations of the studied compositions are thermoactivation processes, we calculated the activation energies based on the experimental data of the relaxation time using the Arrhenius law [49]:

$$\tau = \tau_0 \exp\left(\frac{E_a}{k_B T}\right) \quad (6)$$

where τ_0 —preexponential factor, E_a —activation energy, k_B —Boltzmann constant, T is the absolute temperature. The corresponding diagrams of the dependencies of the activation energies on temperature for the reference and mechanically activated samples are shown in Fig. 9.

Fig. 8 Frequency dependencies of real $M'(\omega)$ and imaginary $M''(\omega)$ parts of the electric modulus of the reference (a), (b) and mechanically activated (a'), (b') $\text{PbZr}_{0.7}\text{Ti}_{0.3}\text{O}_3$ ceramics at 240 MPa

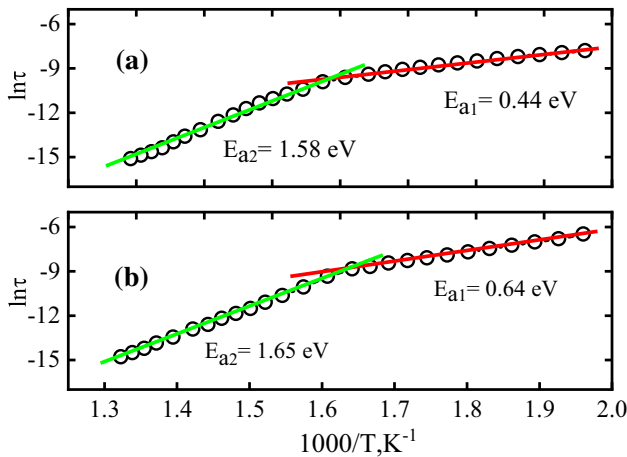
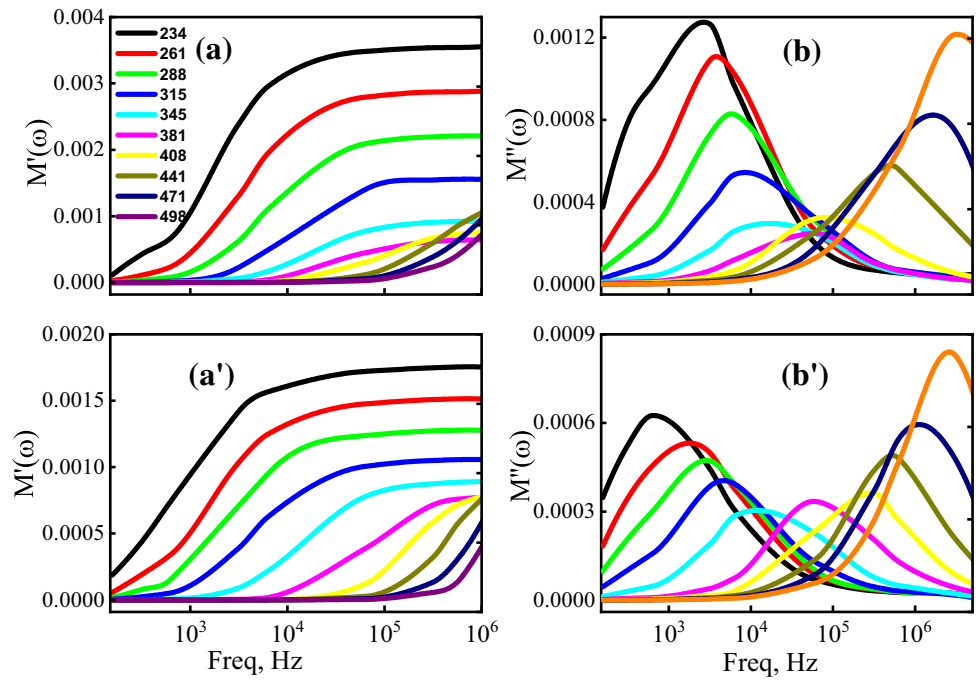


Fig. 9 Dependencies of the activation energies of the reference (a) and mechanically activated (b) $\text{PbZr}_{0.7}\text{Ti}_{0.3}\text{O}_3$ ceramics at 240 MPa

Figure 9 shows two temperature regions with different activation energies E_a . The activation energies of the first temperature region are 0.44 eV for the reference and 0.64 eV for the mechanically activated samples. In titanates, such activation energies are associated with jumps of conduction electrons. The second temperature region is characterized by the following activation energies: 1.58 eV for the reference and 1.65 eV for the mechanically activated samples. These activation energies are due to the movement of oxygen vacancies [50, 51]. As shown in Table 4, the mechanical activation leads to non-monotonic changes in the activation energies of $\text{Pb}(\text{Zr}_{0.7}\text{Ti}_{0.3})\text{O}_3$.

Table 4 Dependencies of the activation energies of the $\text{Pb}(\text{Zr}_{0.7}\text{Ti}_{0.3})\text{O}_3$ on the mechanical activation pressure

P , MPa	E_{a1} , eV	E_{a2} , eV
0	0.443	1.586
80	0.464	1.594
120	0.726	1.530
160	0.820	1.424
200	0.816	1.539
240	0.639	1.650
320	0.789	1.846

It was also of interest to study the influence of structural defects on the type of phase transition. For this purpose, we have studied ($f=1$ MHz) the dependencies of the Weiss constant C_w and the temperature difference $T_m - T_w$ on the mechanical activation pressure. The second quantity can act as a “primacy criterion” for phase transitions in PZT solid solutions. For the calculation, we used the formula [29, 52]:

$$\epsilon = \frac{C_w}{T - T_w} \tag{7}$$

where C_w —the Weiss constant, T_w —the Curie–Weiss temperature, T —the temperature in the linear section of the dielectric constant. The dependencies of these parameters on the mechanical activation pressures are shown in Fig. 10.

As shown in Fig. 10, the $C_w(P)$ dependency is non-monotonic, and the temperature difference $T_m - T_w$ decreases with increasing the mechanical activation pressure. Therefore, the phase transition becomes closer to a second-order phase transition.

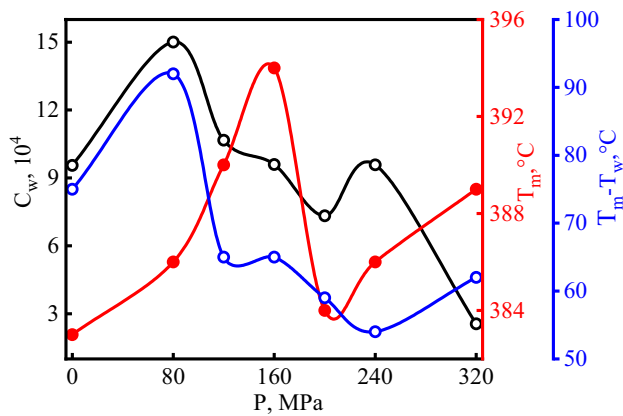


Fig. 10 The Weiss constant C_w and the temperature difference $T_m - T_w$ of $\text{PbZr}_{0.7}\text{Ti}_{0.3}\text{O}_3$ ceramics dependencies on the mechanical activation pressures

4 Conclusion

The results obtained in this work: studying the influence of mechanical activation on pre-synthesized $\text{PbZr}_{0.7}\text{Ti}_{0.3}\text{O}_3$ powders shows the possibility of controlling many physical properties of the powder and ceramic samples. Although the sintering of ceramics from mechanically activated powders in various metastable states is a high-temperature treatment of densely compacted workpieces, the experimental results and their comparison with the reference sample show that during ceramic sintering, some structural defects disappear, and some remain in the ceramics.

Structural defects have been found to affect different physical properties in different ways.

The small size of the coherent scattering regions of mechanically activated powders also plays a significant role in forming the physical properties of the $\text{Pb}(\text{Zr}_{0.7}\text{Ti}_{0.3})\text{O}_3$ ceramics. Depending on the crystallite size that enters into a chemical reaction during ceramic sintering, the diffusion zone can have a different shape (concave, convex, etc.), and the reactions themselves are described by different temperature–time laws. All these conclusions and generalizations given above can be applied to many mechanically activated crystalline bodies.

Acknowledgements Research was financially supported by the Ministry of Science and Higher Education of the Russian Federation (State assignment in the field of scientific activity, No. 0852-2020-0019).

Declarations

Conflict of interest The authors declare that they have no known competing financial interests or personal relationships that could have appeared to influence the work reported in this paper.

References

1. K.G. Abdulvakhidov, E.N. Ubushaeva, I.V. Mardasova, M.A. Vitchenko, B.K. Abdulvakhidov, V.G. Zaletov, A.A. Amirov, I.K. Kamilov, A.S. Manukyan, P.S. Plyaka, G.B. Sukharina, *Ferroelectrics* **494**, 182 (2016)
2. K.G. Abdulvakhidov, M.A. Vitchenko, I.V. Mardasova, E.N. Oshaeva, *Tech. Phys.* **53**, 661 (2008)
3. E.N. Ubushaeva, K.G. Abdulvakhidov, I.V. Mardasova, B.K. Abdulvakhidov, M.A. Vitchenko, A.A. Amirov, A.B. Batdalov, A.G. Gamzatov, *Tech. Phys.* **55**, 1596 (2010)
4. M.A. Vitchenko, I.V. Mardasova, É.N. Oshaeva, K.G. Abdulvakhidov, E.Y. Faïn, *Tech. Phys. Lett.* **33**, 160 (2007)
5. E. Gaffet, D. Michel, L. Mazerolles, P. Berthet, *Mater. Sci. Forum* **235–238**, 103 (1996)
6. V. Šepelák, U. Steinike, D.C. Uecker, S. Wißmann, K.D. Becker, *J. Solid State Chem.* **135**, 52 (1998)
7. T.D. Shen, C.C. Koch, T.L. McCormick, R.J. Nemanich, J.Y. Huang, J.G. Huang, *J. Mater. Res.* **10**, 139 (1995)
8. H.J. Fecht, *Nature* **356**, 133 (1992)
9. G.J. Fan, F.Q. Guo, Z.Q. Hu, M.X. Quan, K. Lu, *Phys. Rev. B* **55**, 11010 (1997)
10. B. Bokhonov, I. Konstanchuk, E. Ivanov, V. Boldyrev, *J. Alloys Compd.* **187**, 207 (1992)
11. B. Bokhonov, I. Konstanchuk, V. Boldyrev, E. Ivanov, *J. Non. Cryst. Solids* **153–154**, 606 (1993)
12. D.L. Polla, L.F. Francis, *MRS Bull.* **21**, 59 (1996)
13. J.F. Scott, *Ferroelectrics* **236**, 247 (2000)
14. C.T. Lin, B.W. Scanlan, J.D. McNeill, J.S. Webb, L. Li, R.A. Lipeles, P.M. Adams, M.S. Leung, *J. Mater. Res.* **7**, 2546 (1992)
15. S. Yokoyama, Y. Ito, K. Ishihara, K. Hamada, S. Ohnishi, J. Kudo, K. Sakiyama, *Jpn. J. Appl. Phys.* **34**, 767 (1995)
16. N. Neumann, R. Köhler, G. Hofmann, *Integr. Ferroelectr.* **6**, 213 (1995)
17. K.R. Mohana Rao, A.V.P. Rao, S. Komarneni, *Mater. Lett.* **28**, 463 (1996)
18. R.N. Das, A. Pathak, P. Pramanik, *J. Am. Ceram. Soc.* **81**, 3357 (1998)
19. V.R. Palkar, M.S. Multani, *Mater. Res. Bull.* **14**, 1353 (1979)
20. H. Hirashima, E. Onishi, M. Nakagawa, *J. Non. Cryst. Solids* **121**, 404 (1990)
21. T.R.N. Kutty, R. Balachandran, *Mater. Res. Bull.* **19**, 1479 (1984)
22. T.R. Shrout, P. Papet, S. Kim, G.-S. Lee, *J. Am. Ceram. Soc.* **73**, 1862 (1990)
23. C.A. Randall, N. Kim, J.-P. Kucera, W. Cao, T.R. Shrout, *J. Am. Ceram. Soc.* **81**, 677 (1998)
24. S. Samanta, V. Sankaranarayanan, K. Sethupathi, *Vacuum* **156**, 456 (2018)
25. B. Jaffe, W.R. Cook, H. Jaffe, in *Piezoelectric Ceram.* (Elsevier, 1971), pp. 135–183.
26. M.R.R. Soares, A.M.R.M.R. Senos, P.Q.Q. Mantas, *J. Eur. Ceram. Soc.* **20**, 321 (2000)
27. N.K. James, U. Lafont, S. van der Zwaag, W.A. Groen, *Smart Mater. Struct.* **23**, 055001 (2014)
28. F. Van Loock, D.B. Deutz, S. van der Zwaag, W.A. Groen, *Smart Mater. Struct.* **25**, 085039 (2016)
29. M.A. Sirota, K.G. Abdulvakhidov, *J. Surf. Investig. X-Ray, Synchrotron Neutron Tech.* **11**, 677.
30. M. Sirota, K. Abdulvakhidov, T. Lastovina, A. Pnevskaya, E. Ubushaeva, P. Plyaka, A. Nazarenko, M. Vitchenko, I. Mardasova, A. Budnyk, *Phys. Status Solidi* **218**, 2000782 (2021)
31. R.Z. Valiev, I.V. Alexandrov, *Nanostructured Mater.* **12**, 35 (1999)
32. K. Abdulvakhidov, A. Soldatov, I. Dmitrenko, Z. Li, S. Kallaev, Z. Omarov, *Results Phys.* **22**, 103905 (2021)

33. D.M. Vasil'ev and B.I. Smirnov, *Sov. Phys. Uspekhi* **4**, 226 (1961).
34. H.P. Rooksby, *Acta Crystallogr.* **19**, 489 (1965)
35. M.A. Sirota, K.G. Abdulvakhidov, A.P. Budnyk, A.V. Soldatov, A.L. Bugaev, T.A. Lastovina, Y.V. Kabirov, M.I. Mazuritskiy, P.S. Plyaka, S.N. Kallaev, Z.M. Omarov, S.A. Sadykov, B.K. Abdulvakhidov, I.V. Mardasova, M.A. Vitchenko, *Ferroelectrics* **526**, 1 (2018)
36. J. Tauc, R. Grigorovici, A. Vancu, *Phys. Status Solidi* **15**, 627 (1966)
37. F. Wooten, in *Opt. Prop. Solids*, edited by F. Wooten (Elsevier, 1972), pp. 42–84.
38. E.A. Davis, N.F. Mott, *Philos. Mag.* **22**, 903 (1970)
39. J.T. Last, *Phys. Rev.* **105**, 1740 (1957)
40. C.A. Guarany, L.H.Z. Peláio, E.B. Araújo, K. Yukimitu, J.C.S. Moraes, and J.A. Eiras, *J. Phys. Condens. Matter* **15**, 4851 (2003).
41. E.B. Araújo, C.A. Guarany, K. Yukimitu, J.C.S. MORAES, and J.A. Eiras, *Ferroelectrics* **337**, 145 (2006).
42. C.H. Perry, B.N. Khanna, G. Rupprecht, *Phys. Rev.* **135**, A408 (1964)
43. E.B. Wilson, J.C. Decius, and P.C. Cross, *Molecular Vibrations: The Theory of Infrared and Raman Vibrational Spectra* (Courier Corporation, 1980).
44. V.V. Lemanov, A.V. Sotnikov, E.P. Smirnova, M. Weihnacht, *Phys. Solid State* **44**, 2039 (2002)
45. P. Lunkenheimer, V. Bobnar, A.V. Pronin, A.I. Ritus, A.A. Volkov, A. Loidl, *Phys. Rev. B* **66**, 052105 (2002)
46. A.V. Turik, G.S. Radchenko, A.I. Chernobabov, S.A. Turik, V.V. Suprunov, *Phys. Solid State* **48**, 1157 (2006)
47. F. Borsa, D.R. Torgeson, S.W. Martin, H.K. Patel, *Phys. Rev. B* **46**, 795 (1992)
48. H. Jain, C. Hsieh, *J. Non. Cryst. Solids* **172–174**, 1408 (1994)
49. K. Manjunatha, V. Jagadeesha Angadi, K. M. Srinivasamurthy, S. Matteppanavar, V. K. Pattar, and U. Mahaboob Pasha, *J. Supercond. Nov. Magn.* **33**, 1747 (2020).
50. C. Ang, Z. Yu, L.E. Cross, *Phys. Rev. B* **62**, 228 (2000)
51. D.M. Smyth, *Curr. Opin. Solid State Mater. Sci.* **1**, 692 (1996)
52. K. Manjunatha, V.J. Angadi, R.A.P. Ribeiro, M.C. Oliveira, S.R. de Lázaro, M.R.D. Bomio, S. Matteppanavar, S. Rayaprol, P.D. Babu, U.M. Pasha, *New J. Chem.* **44**, 14246 (2020)

Publisher's Note Springer Nature remains neutral with regard to jurisdictional claims in published maps and institutional affiliations.